

Escaping the Diversity Trap in Robotic Manipulation via Anchor-Centric Adaptation

Yanzhe Chen¹ Kevin Yuchen Ma^{1,2} Qi Lv^{1,3} Yiqi Lin¹ Zechen Bai¹ Chen Gao¹ Mike Zheng Shou¹

Abstract

While Vision-Language-Action (VLA) models offer broad general capabilities, deploying them on specific hardware requires real-world adaptation to bridge the embodiment gap. Since robot demonstrations are costly, this adaptation must often occur under a strict data budget. In this work, we identify a critical **diversity trap**: the standard heuristic of “maximizing coverage” by collecting diverse, single-shot demonstrations can be self-defeating due to non-vanishing estimation noise. We formalize this phenomenon as a **Coverage–Density Trade-off**. By decomposing the policy error into estimation (density) and extrapolation (coverage) terms, we characterize an interior optimal allocation of unique conditions for a fixed budget. Guided by this analysis, we propose **Anchor-Centric Adaptation (ACA)**, a two-stage framework that first stabilizes a policy skeleton through repeated demonstrations at core anchors, then selectively expands coverage to high-risk boundaries via teacher-forced error mining and constrained residual updates. Real-robot experiments validate our trade-off framework and demonstrate that ACA significantly improves task reliability and success rates over standard diverse sampling strategies under the same budget.

1. Introduction

I fear not the man who has practiced 10,000 kicks once, but I fear the man who has practiced one kick 10,000 times. – Bruce Lee

Vision–Language–Action (VLA) models have demonstrated broad capabilities from pretraining (Zitkovich et al., 2023; Black et al., 2025; Bu et al., 2025). However, deploying

¹National University of Singapore ²Institute for Information Research, A*STAR ³Harbin Institute of Technology (Shenzhen). Correspondence to: Mike Zheng Shou <mike.zheng.shou@gmail.com>.

Preprint. May 11, 2026.

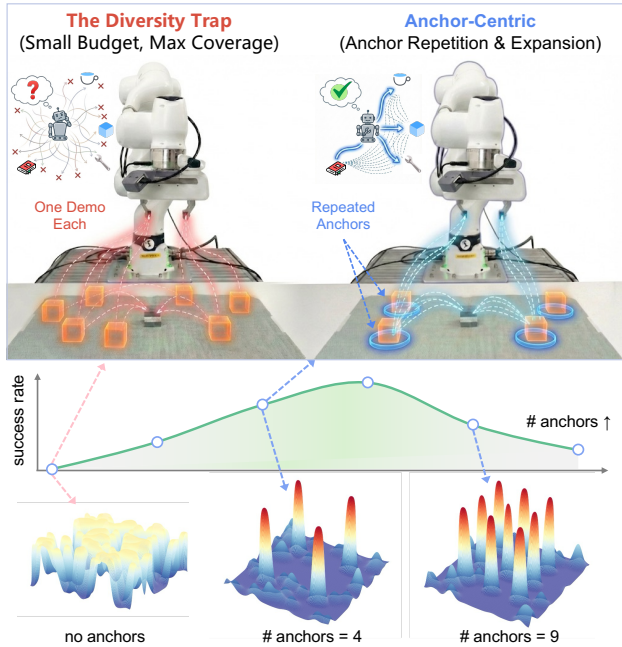


Figure 1. **Illustration of Motivation.** **Top:** Contrasting the “diversity trap” of sparse, single-shot sampling against stable anchor-centric repetition. **Middle & Bottom:** Inverted-U trend of success versus number of anchors, with 3D visualizations of sample distributions and densities at representative points.

these models on specific physical platforms remains a challenge due to the embodiment mismatch and subtle environmental shifts that create substantial distribution gaps (Kawaharazuka et al., 2025; Zhang et al., 2025b). Consequently, real-robot post-training is often a prerequisite for reliable deployment (Xiang et al., 2025; Tan et al., 2025). However, collecting real-world demonstrations is expensive, restricting adaptation to tight data budgets—typically spanning only tens to hundreds of trajectories (Kim et al., 2024; Li et al., 2025a; Chopra et al., 2025). This raises a pivotal question: **Under a limited budget, what is the most effective data collection strategy to learn a robust policy?**

A common approach prioritizes **coverage**—collecting demonstrations across the widest possible array of task conditions to maximize generalizations (Li et al., 2025b; Hou et al., 2025). While this “maximize coverage” heuris-

tic aligns with standard data-scaling narratives (Liu et al., 2023), we identify it as a **diversity trap** in low-budget regimes. Spreading scarce samples too thin leaves each condition under-represented, thereby inflating estimation variance and destabilizing the resulting vector field. In these scenarios, the fundamental challenge shifts from **what to cover** to **how to allocate**.

Our core insight is that budget-efficient adaptation requires **deliberate repetition before expansion**. This principle echoes the concept of **anchoring**: establishing a sparse set of canonical conditions, or anchors, sampled repeatedly to consolidate a stable “policy skeleton”. Empirically, we observe that task success follows an **inverted-U** dependence on the number of anchors. Beyond an optimal point, increasing diversity erodes per-condition density, leading to a catastrophic collapse in policy stability (Fig. 1, bottom).

To formalize this phenomenon, we characterize real-robot post-training as a **Coverage–Density Trade-off**. Under a fixed budget, increasing the number of distinct conditions improves coverage but reduces local sample density, creating a tension between **extrapolation bias** (from unseen regimes) and **estimation noise** (from sparse observations). By analyzing conditional action vector fields (Lipman et al., 2022), we derive a worst-case error bound that explicitly decomposes into these terms. This derivation proves the existence of an **interior optimal allocation**, challenging the optimality of uniform diverse sampling under data scarcity.

Building on this framework, we propose Anchor-Centric Adaptation (ACA), a two-stage framework that navigates this trade-off. **Stage 1 (Anchor-Centric Stabilization)** prioritizes estimation stability by concentrating the budget on a minimal set of anchors, consolidating a low-variance base policy. **Boundary Mining via Teacher-Forced Deviation** then utilizes the base policy’s field error as a proxy for extrapolation risk, efficiently identifying under-supported boundary regimes. Finally, **Stage 2 (Constrained Residual Adaptation)** integrates boundary-specific knowledge via a *parameter-efficient residual pathway*. This additive adaptation enables the model to rapidly incorporate critical data from identified boundaries while preventing performance degradation on the previously consolidated core. On real-robot platforms, ACA significantly improves adaptation robustness and task success, demonstrating the necessity of structured data allocation in the small-budget regime.

Our contributions are summarized as follows:

- **Empirical Insight:** We identify the **diversity trap** in VLA post-training, demonstrating that maximizing coverage under tight budgets destabilizes learning, evidenced by a characteristic inverted-U performance trend.
- **Theoretical Formalization:** We introduce the **Coverage–Density Trade-off** framework, providing an analytical

bound that reveals the optimal sampling density required to balance estimation and extrapolation bias.

- **Practical Framework:** We propose ACA, a two-stage approach employing error-driven boundary acquisition and constrained residual adaptation, improving task success in data-scarce real-robot experiments.

2. Related Work

2.1. Vision-Language-Action (VLA) Models

VLA models unify perception, instruction following, and control by coupling large-scale vision–language pretraining with action prediction, yielding strong semantic generalization and zero-/few-shot transfer in robotics settings (Zitkovich et al., 2023; Bjorck et al., 2025; Li et al., 2024a; Black et al., 2024; Kawaharazuka et al., 2025; Mu et al., 2023; Ahn et al., 2022; Chen et al., 2025). A prominent line treats actions as tokens within an autoregressive multimodal model, enabling web-scale knowledge to shape robot behavior (Kim et al., 2024; Cen et al., 2025b; Pertsch et al., 2025; Zhang et al., 2026). More recent VLAs move toward continuous-time / high-rate control by generating action trajectories with diffusion- or flow-based policies, improving smoothness and temporal fidelity while retaining the benefits of large-scale pretraining (Black et al., 2025; Zhang et al., 2025d; Cen et al., 2025a; Jiang et al., 2025; Shukor et al., 2025; Zhong et al., 2025). Large cross-embodiment datasets and open-source generalist policies further accelerate VLA scaling, evaluation, and downstream adaptation (O’Neill et al., 2024; Zhang et al., 2025a; Li et al., 2024b; Team et al., 2025; Fei et al., 2025).

2.2. Real-World VLA Adaptation

Adapting pretrained VLAs to a new scene typically requires in-domain trajectories to bridge embodiment mismatch and subtle distribution shift, motivating data-efficient post-training pipelines (Kim et al., 2025; Team et al., 2024; Lin et al., 2025; Lee et al., 2025; Kachaev et al., 2025; Li et al., 2025c; Zhao et al., 2025; Mark et al., 2024). A standard heuristic is to maximize condition diversity, but small budgets amplify optimization variance and can render fine-tuning brittle when demonstrations are sparse per condition (Sridhar et al., 2025; Yang et al., 2025). Recent adaptation methods explore parameter-efficient updates, modularity, and constrained refinement to improve robustness (Zhang et al., 2025e; Ni et al., 2025; Wen et al., 2025; Zhang et al., 2025c). Parallel work views adaptation through the lens of continual learning, seeking to prevent catastrophic forgetting while acquiring new skills (Römer et al., 2026; Garcia et al., 2025; Zheng et al., 2025; Hafez & Wermtner, 2023). However, most of these approaches are agnostic to the *acquisition strategy* of the new data itself.

Active or error-driven data collection has also been investigated to prioritize demonstrations that provide the highest marginal value for downstream success under limited budgets (Zhu et al., 2025; Yu et al., 2025; Xue et al., 2025; Wu et al., 2025; Gao et al., 2025; Wang et al., 2023; Zhu et al., 2022; Wang et al., 2024). We introduce a *Coverage–Density trade-off* that explains when “maximize coverage” fails. We bridge this gap with ACA to ensure policy skeleton stability before expanding coverage to high-risk regimes.

3. Coverage–Density Trade-off

This section formalizes the **Coverage–Density Trade-off** inherent in real-robot adaptation under tight data budgets. We analyze the adaptation process as learning a time-dependent conditional vector field via flow-matching (Lipman et al., 2022). Our analysis yields: (i) an error bound decomposing into *density (estimation)* and *coverage (extrapolation)* terms; (ii) an interior optimal allocation K^* that identifies the suboptimality of fully diverse sampling; and (iii) a theoretical foundation for the ACA pipeline. Below we outline the key steps; the complete analysis is provided in § A.1.

3.1. Problem Formulation

Let $p \in \mathcal{P} \subset \mathbb{R}^d$ parameterize geometric variations (e.g., object pose) and $t \in [0, 1]$ denote flow time. The training target is a conditional vector field $f^*(z, p, t)$, where $z \in \mathcal{Z}$ is the action-state. We consider post-training under a *fixed and small* total budget of N samples / trajectories collected at conditions $\{p\}$. A sampling strategy specifies (i) a set of K distinct conditions (**coverage**) and (ii) the number of repeats per condition (**density**) $\{n_i\}_{i=1}^K$ with $\sum_{i=1}^K n_i = N$. Abstracting the flow-matching objective, we consider the regression target:

$$y = f^*(z, p, t) + \varepsilon, \quad \varepsilon \sim \text{sub-Gaussian}(\sigma^2), \quad (1)$$

where ε represents effective noise due to stochasticity and unmodeled effects in real-robot adaptation.

3.2. Assumptions

To make the allocation trade-off explicit, we analyze an idealized **nearest-anchor surrogate**. While deep neural policies are globally parameterized, under small budgets the learning signal is primarily supported by the vicinities of observed conditions, motivating a locality-based analysis.

A1 (Smoothness in Condition). For all (z, t) , $f^*(z, \cdot, t)$ is L -Lipschitz on \mathcal{P} :

$$\|f^*(z, p, t) - f^*(z, p', t)\| \leq L\|p - p'\|. \quad (2)$$

A2 (Effective Local Estimation). For fixed (z, t) , the effective estimation error at an observed condition p_i de-

creases with its repeat count n_i :

$$\mathbb{E}\|\hat{f}(z, p_i, t) - f^*(z, p_i, t)\| \leq \frac{C\sigma}{\sqrt{n_i}}, \quad (3)$$

where $C > 0$ is a universal constant. This abstracts the empirically observed variance reduction from repeated supervision; global parameter sharing may affect constants but preserves the $1/\sqrt{n_i}$ dependence.

A3 (Surrogate Generalization). For analysis we consider a local predictor that queries the nearest observed condition:

$$\hat{f}(z, p, t) := \hat{f}(z, p_{i(p)}, t), \quad i(p) = \arg \min_i \|p - p_i\|. \quad (4)$$

We emphasize that A3 is an *idealized locality surrogate* used to make the coverage term explicit and to expose worst-case dependence on the fill distance h . Deep policies may interpolate more smoothly than this surrogate; our claims focus on the *mechanism* of the coverage–density trade-off and the resulting interior optimum, rather than a tight characterization of neural-network generalization.

3.3. The Coverage–Density Decomposition

Define the *fill distance*

$$h := \sup_{p \in \mathcal{P}} \min_i \|p - p_i\|, \quad (5)$$

representing the worst-case coverage gap in \mathcal{P} .

Proposition 3.1 (Coverage–Density Bound). *Under A1–A3, the worst-case expected field error is bounded by:*

$$\sup_{p, z, t} \mathbb{E}\|\hat{f} - f^*\| \leq \underbrace{\max_i \mathbb{E}\|\hat{f}_i - f_i^*\|}_{\text{Estimation (Density) Error}} + \underbrace{Lh}_{\text{Extrapolation Bias}}, \quad (6)$$

where $\hat{f}_i := \hat{f}(z, p_i, t)$ and $f_i^* := f^*(z, p_i, t)$.

Proof sketch. For any p , let $p_{i(p)}$ be its nearest anchor. By A3, $\hat{f}(z, p) = \hat{f}(z, p_{i(p)})$. Let $\Delta(z, p) = \|\hat{f}(z, p) - f^*(z, p)\|$ denote the policy error at point p . By the triangle inequality and Assumption A3, the error can be bounded as:

$$\Delta(z, p) \leq \Delta(z, p_{i(p)}) + \|f^*(z, p_{i(p)}) - f^*(z, p)\|. \quad (7)$$

The second term is bounded by $L\|p - p_{i(p)}\| \leq Lh$ via A1. Taking expectation and supremum over p yields Proposition 3.1. \square

3.4. Scaling Law & The Diversity Trap

To obtain a simple scaling law, we analyze quasi-uniform anchor placement and uniform repeats.

Lemma 3.2 (Uniform allocation with quasi-uniform anchors). *Assume (i) uniform repeats $n_i = N/K$ for all anchors, and (ii) quasi-uniform anchor placement on \mathcal{P} such that $h \leq cK^{-1/d}$ for some constant $c > 0$. Then*

$$\mathcal{E}(K) := \sup_{p \in \mathcal{P}} \mathbb{E} \|\hat{f} - f^*\| \leq C\sigma \sqrt{\frac{K}{N}} + LcK^{-1/d}. \quad (8)$$

Proof sketch. By A2 and $n_i = N/K$, $\max_i \mathbb{E} \|\hat{f}(z, p_i, t) - f^*(z, p_i, t)\| \leq C\sigma \sqrt{K/N}$. By assumption, $h \leq cK^{-1/d}$. Plug into Proposition 3.1. \square

Corollary 3.3 (Interior Optimal Allocation). *Under non-negligible noise $\sigma > 0$, the error $\mathcal{E}(K)$ is minimized at an interior optimal K^* :*

$$K^* = \left(\frac{2LcN^{1/2}}{dC\sigma} \right)^{\frac{2d}{d+2}} \propto \left(\frac{L^2N}{\sigma^2} \right)^{\frac{d}{d+2}} < N, \quad (9)$$

for sufficiently large N . At this choice,

$$\mathcal{E}(K^*) = \tilde{O}\left(\sigma^{\frac{2}{d+2}} L^{\frac{d}{d+2}} N^{-\frac{1}{d+2}}\right), \quad (10)$$

up to constants (C, c) .

Fully diverse sampling. The ‘‘maximize coverage’’ heuristic corresponds to $(K = N, n_i = 1)$, giving

$$\mathcal{E}(N) \leq C\sigma + LcN^{-1/d}, \quad (11)$$

whose leading estimation noise $C\sigma$ **remains constant**. Thus, under non-negligible noise and tight budgets, pushing K toward N is asymptotically suboptimal; repetition is required to reduce estimation error.

3.5. Trajectory Propagation & Two-Stage Motivation

To connect vector-field accuracy to task behavior, let $z(t)$ and $\hat{z}(t)$ be trajectories induced by $f^*(\cdot, p, \cdot)$ and $\hat{f}(\cdot, p, \cdot)$ from the same initial condition. Assuming both fields are Λ -Lipschitz in z over a bounded domain \mathcal{Z} , Grönwall’s inequality (Evans, 2022) implies:

$$\|\hat{z}(T) - z(T)\| \leq \frac{e^{\Lambda T} - 1}{\Lambda} \cdot \delta(p), \quad (12)$$

where $\delta(p) = \sup_{z,t} \|\hat{f}(z, p, t) - f^*(z, p, t)\|$. Eq. (12) motivates using field-approximation error as a proxy for open-loop deviation: errors can be amplified along the trajectory as T increases. Since Proposition 3.1 is stated in expectation and pointwise in (z, t) , in the main text we use Lemma 3.2 as a conservative proxy to reason about regimes where extrapolation dominates (large h), which predicts larger open-loop deviation and lower success. A uniform high-probability version over bounded (z, t) domains is provided in the supplement.

Proposition 3.1 directly suggests a two-stage allocation under a fixed budget. Repeating a small set of anchor conditions reduces the estimation (density) term, while adding a small number of additional conditions reduces the extrapolation (coverage) term in regions far from anchors. Let $\mathcal{P}_{\text{bd}} \subset \mathcal{P}$ denote such boundary regimes and

$$h_{\text{bd}} := \sup_{p \in \mathcal{P}_{\text{bd}}} \min_i \|p - p_i\|. \quad (13)$$

When h_{bd} is large, boundary error is dominated by Lh_{bd} ; thus it is most efficient to (i) stabilize learning via repeated anchors, then (ii) selectively expand to boundary conditions identified by a deviation-correlated signal (Eq. 12) and update the policy with a parameter-efficient residual correction to limit unnecessary drift on anchors.

4. Anchor-Centric Adaptation (ACA)

We introduce **ACA**, a two-stage framework that operationalizes the coverage–density trade-off for budget-efficient VLA adaptation (Fig. 2). ACA sequences the adaptation process into: (i) anchor densification for core stabilization, and (ii) error-guided expansion for boundary competence.

4.1. Architectural Preliminaries

ACA builds upon a flow-based VLA architecture (Black et al., 2024; 2025), which decouples perception and action through a pretrained *VLM* and a task-specific *Action Expert*. The policy is trained by flow matching to learn a time-dependent action vector field conditioned on the task condition p and flow time $\tau \in [0, 1]$.

Theoretical Mapping. Our analysis in Sec. 3 studies field approximation *pointwise* at fixed action-state and flow time, which makes the coverage–density mechanism explicit. ACA instantiates the resulting core-to-boundary allocation in a practical pipeline.

Budget Allocation. Given a strict total budget of N real-robot trajectories, ACA partitions the interaction into three functional stages:

$$N = N_{\text{A}} + N_{\text{probe}} + N_{\text{bd}}, \quad (14)$$

where N_{A} trajectories are dedicated to core anchoring, N_{probe} trajectories serve as a screening pool for boundary identification, and N_{bd} trajectories provide the expansion.

4.2. Stage 1: Anchor-Centric Stabilization

Stage 1 seeks to reduce *estimation variance* by concentrating the majority of the interaction budget on a sparse set of core anchors $\{p_i\}_{i=1}^K$.

Anchoring Strategy. Anchors are selected to form a coarse, quasi-uniform cover of the reachable workspace. We collect

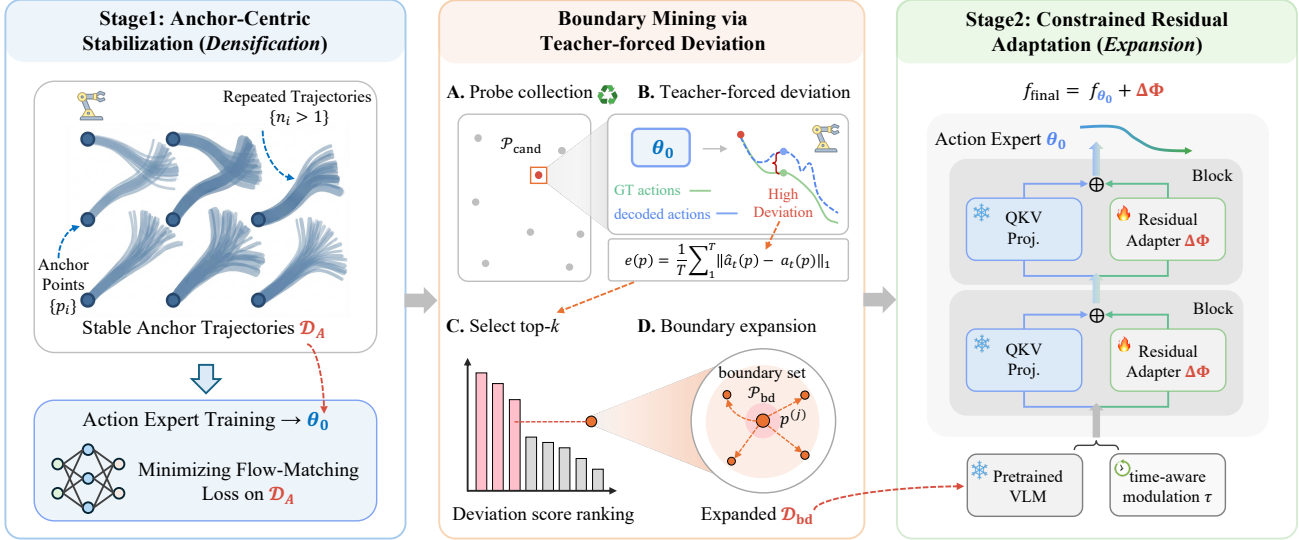


Figure 2. **Overview of Anchor-Centric Adaptation (ACA).** Stage 1 learns a stable core policy by repeating demonstrations at sparse anchors; **Boundary mining** screens probe trajectories and selects high-deviation locations; **Stage 2** expands boundary competence via a constrained, parameter-efficient residual update in the *Action Expert*, while keeping the pretrained VLM frozen.

repeated demonstrations at each anchor ($n_i > 1$), and train a stable core policy θ_0 .

Training. We train the Action Expert on the anchor dataset \mathcal{D}_A using the standard flow-matching objective:

$$\theta_0 = \arg \min_{\theta} \mathbb{E}_{(a,p) \sim \mathcal{D}_A} [\mathcal{L}_{\text{FM}}(\theta; a, p)], \quad (15)$$

while keeping the VLM frozen to leverage pretrained multimodal representations. This stage yields a policy that is reliable in well-supported regions but may still incur extrapolation error in under-sampled boundary regimes.

4.3. Boundary Mining via Teacher-Forced Deviation

Boundary mining identifies under-supported regimes where the Stage-1 policy is likely to extrapolate poorly.

Deviation-Based Screening. We first collect a set of *probe* trajectories by teleoperation at conditions sampled across the workspace, forming a candidate set $\mathcal{P}_{\text{cand}}$ (one probe trajectory per candidate condition). For each candidate condition $p \in \mathcal{P}_{\text{cand}}$, we compute a **teacher-forced deviation score** by decoding actions on the *demonstration* observation sequence and comparing to the demonstrated actions:

$$e(p) := \frac{1}{T} \sum_{t=1}^T \|\hat{a}_t(p) - a_t(p)\|_1. \quad (16)$$

Teacher forcing avoids compounding state drift, making $e(p)$ a clean proxy for action prediction error at condition p .

Selecting high-deviation locations. We select boundary locations using a top- k rule for robustness and simplicity: we take the k candidates with the largest deviation scores.

Denote the selected set as $\mathcal{P}_{\text{bd}} = \{p^{(j)}\}_{j=1}^k$. Crucially, the corresponding k probe trajectories are *reused* as boundary supervision in Stage 2.

Local boundary expansion. Around each selected boundary location $p^{(j)}$, we sample nearby conditions (e.g., random perturbations within a small neighborhood) and collect additional trajectories, forming an expanded boundary dataset. This targeted expansion selectively reduces the coverage gap in regimes most detrimental to task success.

4.4. Stage 2: Constrained Residual Adaptation

Boundary training set. Stage 2 trains on a boundary dataset \mathcal{D}_{bd} that combines (i) the reused high-deviation probe trajectories from boundary mining and (ii) the newly collected local-expansion trajectories around \mathcal{P}_{bd} .

Residual Architecture. Stage 2 improves boundary behavior *without* drifting the anchored core from Stage 1. We therefore freeze the Stage-1 policy and introduce a small trainable *residual* branch inside the *Action Expert*. For each training instance with condition p , observation/context, and flow time τ , the model predicts a time-dependent action vector field at a flow-state z . The frozen base policy produces $f_{\theta_0}(z, p, \tau)$, while the residual branch outputs a same-dimensional correction $\Delta_{\phi}(z, p, \tau)$, yielding

$$f_{\text{final}}(z, p, \tau) = f_{\theta_0}(z, p, \tau) + \Delta_{\phi}(z, p, \tau), \quad (17)$$

where θ_0 is fixed and only ϕ is optimized. We parameterize Δ_{ϕ} with low-rank adapters (LoRA) (Hu et al., 2022) inserted into selected linear layers of the Action Expert, constraining updates to a low-capacity subspace. Finally, we

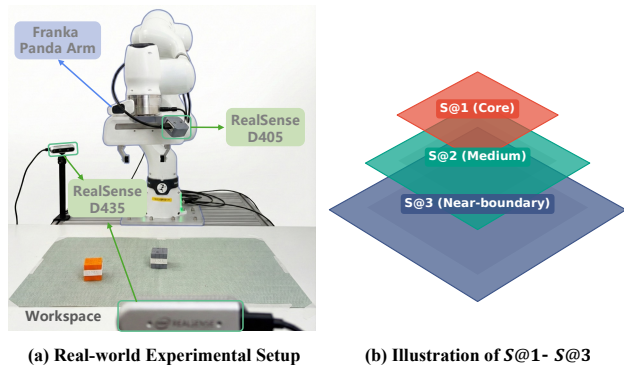


Figure 3. Illustration of (a) the real-robot experimental setup and (b) the spatial definition of $S@1$ - $S@3$.

modulate the residual strength using the flow-time embedding so the correction can specialize across different stages of the denoising process.

Optimization. We optimize only ϕ on the boundary dataset \mathcal{D}_{bd} using the same flow-matching objective as Stage 1, while keeping θ_0 frozen. The residual branch is zero-initialized, so optimization starts exactly from the Stage-1 policy. With a fixed base predictor and a low-rank, time-modulated correction, Stage 2 primarily adds localized capacity for boundary regimes while substantially reducing the risk of global drift typical of full-parameter fine-tuning.

5. Experiment

We evaluate the ACA framework by addressing three objectives: (i) the effectiveness of ACA in mitigating the **diversity trap** and its generalization across VLA backbones; (ii) the sensitivity of adaptation to **anchor properties**, specifically the quantity, spatial layout, and consolidation budget N_A ; and (iii) the individual and joint contributions of **boundary mining** and **residual adaptation** to overall performance.

5.1. Experimental Setup

We evaluate ACA on real hardware to capture the **non-vanishing estimation noise** ($\sigma > 0$) central to our framework (shown in Sec. 3). Unlike simulation environments that often rely on deterministic transitions or simplified noise models (Peng et al., 2018; Chebotar et al., 2019), real-world interactions exhibit stochastic variability critical for characterizing the “diversity trap”. This setting ensures our results reflect the true estimation–extrapolation tension inherent to physical robot adaptation.

Hardware & Data Collection. All tasks are performed on a 7-DoF Franka Panda arm. The workspace is monitored by a multi-view camera system, as shown in Fig. 3 (a) comprising a front and rear-side **RealSense D435**, and a wrist-mounted **D405** for localized observation. We collect demonstrations

via **leader-follower teleoperation** using two identical Panda arms, providing high-fidelity trajectories for both anchor-centric stabilization and boundary expansion.

Tasks. We evaluate ACA on four representative tabletop manipulation tasks that demand high-precision execution across varying workspace regions. (i) *Block Stacking*. Placing a cube onto a target block, requiring the final stack to be stable. (ii) *Cup Placement*. Positioning a cup onto a coaster. (iii) *Table Cleaning*. Using a brush to sweep a block into a dustpan. (iv) *Toy Tidying*. Place toys into a storage box. Real-robot executions of these tasks are shown in Fig. 8.

Metrics. To assess robustness against geometric variation, we define **Region-Level Success Rates ($S@i$)**. Inspired by $\text{Recall}@K$ metrics in information retrieval (Radford et al., 2021; Nogueira & Cho, 2019), we categorize the workspace into three nested rectangular regions of increasing difficulty, as illustrated in Fig. 3 (b): **$S@1$** (core, 25% area), **$S@2$** (medium, 50% area), and **$S@3$** (near-boundary, 90% area). Unless otherwise specified, we sample initial object placements uniformly within each region and report the success rate over 20 evaluation trajectories per task.

Implementation Details. We instantiate ACA using flow-matching VLA policies, specifically π_0 and $\pi_{0.5}$ (Black et al., 2024; 2025). All models are trained using the Adam optimizer with a batch size of 64 on 8 NVIDIA H200 GPUs. Both stages use an action horizon of 16. **Stage 1 (Stabilization).** We train the Action Expert for 20K steps. The learning rate (LR) follows a linear warmup from 0 to 5×10^{-5} over the first 1,500 steps, followed by a cosine decay to 2.5×10^{-5} . **Boundary Mining.** The deviation score $e(p)$ is computed as the L_1 norm averaged across 7 dimensions (position, orientation, and gripper state). The number of mined boundary conditions is budget-dependent, with $k \in \{2, 3, 5\}$ corresponding to interaction budgets of $\{50, 100, 150\}$ trajectories, respectively. **Stage 2 (Adaptation).** We perform 10K steps of residual fine-tuning without warmup. The LR starts at 2.5×10^{-5} and follows a cosine schedule. We employ LoRA with a rank and α of 32.

5.2. Main Results

Experimental Protocol. We compare ACA with the baseline on success rates across three spatial regimes ($S@1$ – $S@3$) under varying data budgets (Table 1). Anchor configuration is fixed to 6 anchors, distributed as the Center Rect type in Fig. 4. **Baseline Definition.** The baseline ($\pi_{0.5}$) uses standard VLA fine-tuning with maximal-diversity sampling: every demonstration is collected at a distinct, non-repeated condition. **Analysis.** (i) *Consistent gains across data scales.* ACA significantly outperforms the diversity-first baseline at every budget level. For a budget of $N = 100$, ACA achieves a 72.5% mean success rate, yielding a +40.8% absolute improvement over the baseline.

Table 1. **Region-level success rates under varying data budgets N .** Reported as: *successful trajectories (out of 20 trials) and mean success rate (%)*. $S@k$ denotes success within progressively larger central regions (harder as k increases).

Method	Block Stacking			Cup Placement			Table Cleaning			Toy Tiding			Mean (%)
	S@1	S@2	S@3	S@1	S@2	S@3	S@1	S@2	S@3	S@1	S@2	S@3	
$N = 50$													
$\pi_{0.5}$	5	2	0	6	4	0	2	0	0	8	4	2	13.8
$\pi_{0.5} + \text{ACA}$	10	12	9	14	10	10	7	6	5	12	10	6	46.3 +32.5
$N = 100$													
$\pi_{0.5}$	8	2	0	14	6	3	10	2	1	14	10	6	31.7
$\pi_{0.5} + \text{ACA}$	16	14	13	18	17	14	12	11	8	18	16	17	72.5 +40.8
$N = 150$													
$\pi_{0.5}$	14	8	4	18	13	8	9	7	4	18	14	10	52.9
$\pi_{0.5} + \text{ACA}$	17	18	16	20	20	18	14	11	9	20	19	19	83.8 +30.9

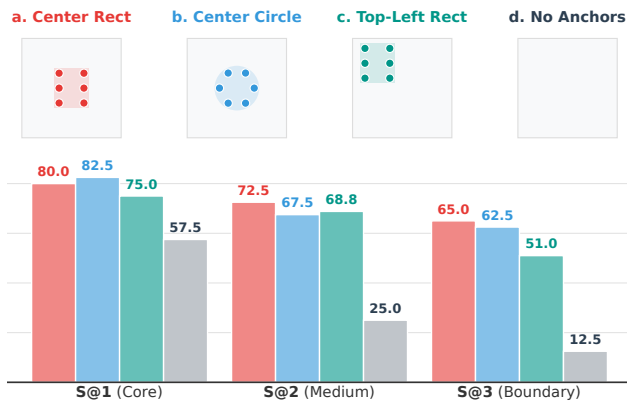


Figure 4. **Sensitivity to anchor spatial distribution.** *Top:* Four configurations (a–d) are evaluated under a fixed budget of $N = 100$. *Bottom:* Region-level success rates across the configurations.

(ii) **Alleviating the diversity trap.** The baseline frequently collapses to zero successes in near-boundary regions (S@3) due to insufficient per-condition density. ACA alleviates this by first stabilizing the policy skeleton; for example, in Block Stacking at $N = 150$, ACA reaches an 80% success rate (16 / 20) compared to only 20% for the baseline. (iii) **Sample efficiency.** ACA exhibits efficiency gains by prioritizing structured repetition. Notably, ACA at the lowest budget ($N = 50$, 46.3% mean) achieves performance comparable to the baseline at triple the budget ($N = 150$, 52.9% mean). (iv) **Robustness to distribution shifts.** As task conditions move from the central core (S@1) to the boundary (S@3), baseline performance drops precipitously. In contrast, ACA maintains higher stability throughout the entire workspace, confirming that anchor-based consolidation provides a more robust foundation for adaptation.

5.3. Ablation Studies

Anchor Spatial Distribution. We examine the impact of anchor spatial distribution by fixing the total budget at

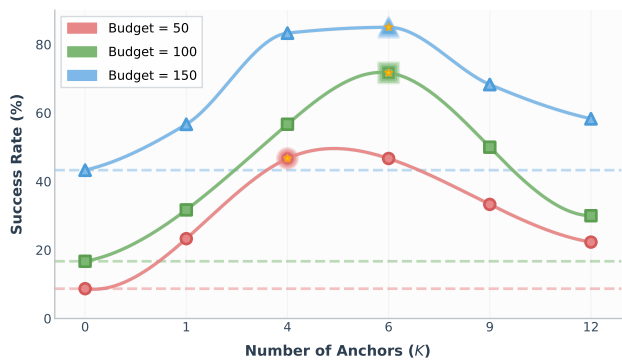


Figure 5. **Sensitivity to the number of anchors (K).** Success rates exhibit a consistent inverted-U trend across different budgets.

$N = 100$ trajectories and the number of anchors at $K = 6$, as shown in Fig. 4. (i) **Necessity of anchoring.** All anchor configurations consistently outperform the baseline across all regions. Notably, even the spatially biased top-left layout yields a $4\times$ **improvement** in boundary (S@3) success (51.0% vs. 12.5%), confirming that a stable policy skeleton is more vital than uniform coverage. (ii) **Centralization and reach.** Centralized anchors (a, b) yield the highest success by minimizing the maximum extrapolation distance to any workspace point. This strategy effectively balances local sampling density with global stability, resulting in the most graceful performance degradation. (iii) **Robustness to geometric patterns.** The performance difference between rectangular and circular arrangements appears to be relatively marginal. This result suggests that the benefits of ACA may be largely invariant to the specific geometric pattern, provided that the anchors maintain a sufficiently centralized distribution to influence the surrounding workspace.

Impact of Anchor Quantity. We evaluate the impact of anchor quantity by varying $K \in \{0, \dots, 12\}$ under a fixed Center Rect layout, as shown Fig. 5. (i) **Observation of the Inverted-U trend.** Across all tested budgets, task success appears non-monotonic with respect to K . This suggests

that the benefits of spatial coverage are effectively bottlenecked by the local sampling density required to suppress estimation noise. *(ii) Validation of the Diversity Trap.* As K increases beyond the optimum, success rates tend to decline despite the broader spatial coverage. This supports our hypothesis that excessive diversity under a fixed budget dilutes the sampling density per condition, potentially leading to the “diversity trap” where estimation noise destabilizes the policy. *(iii) Budget-dependent shift in optimum.* The results suggest that the optimal K may scale with the total interaction budget. For instance, the performance peak broadens as N increases from 50 to 150, which is consistent with our theoretical bound predicting that larger budgets can support higher diversity without sacrificing stability.

Ablation on Boundary Mining and Residual Adaptation.

We fix the total budget at $N = 100$ trajectories with 6 anchors, as shown in Table 2. *(i) Synergy of sampling and architecture.* Combining error-driven mining with residual updates yields the highest mean success rate, showing that robust adaptation requires both identifying critical data gaps and a stable update mechanism. *(ii) Effectiveness of error-driven mining.* Adding the mining phase boosts performance in boundary regions (S@3). Compared to a random-sampling baseline of equal size, error-driven mining raises S@3 success, confirming that teacher-forced deviation reliably locates extrapolation risks. *(iii) Stability via residual updates.* While full-parameter fine-tuning allows for boundary expansion, it results in performance trade-offs in the consolidated core. The residual pathway preserves S@1 & S@2 stability while patching the vector field in under-supported areas.

Table 2. Ablation study of Boundary Mining and Residual Adaptation. Values denote mean success rates across four tasks.

Mining	Residual	S@1	S@2	S@3	Mean
×	×	67.5	58.8	45.0	57.1
×	✓	73.8	62.5	40.0	58.8
✓	×	68.8	66.3	57.5	64.2
✓	✓	80.0	72.5	65.0	72.5

Ablation on Anchor Budget (N_A) Ratio. We examine the trade-off between anchor consolidation and boundary expansion by varying N_A under a fixed budget of $N = 100$, as shown in Fig. 6. *(i) Stabilization as a prerequisite.* Reducing N_A to 50 results in a global performance decline, with core success (S@1) dropping from 80.0% to 65.0%. This outcome validates that an insufficient anchor budget fails to suppress estimation noise, providing a fragile policy skeleton that cannot effectively support subsequent boundary adaptation. *(ii) Optimal budget partitioning.* While $N_A = 100$ maximizes central success (82.5%), allocating $N_A = 80$ trajectories yields the highest overall success (72.5% Mean) and superior boundary performance (65.0%

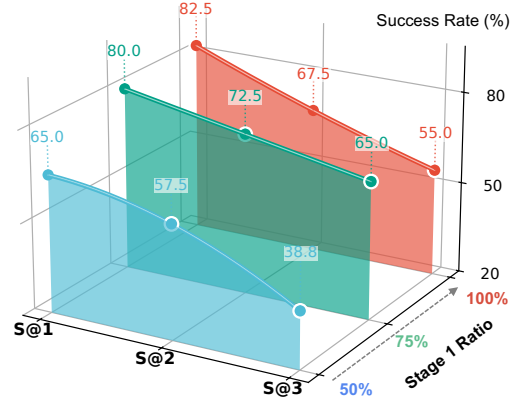


Figure 6. Sensitivity to anchor consolidation budget (N_A). Region-level success rates under a fixed total budget of $N = 100$.

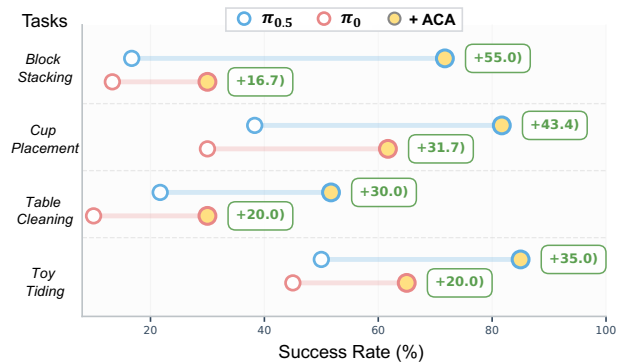


Figure 7. Performance gains across different base VLA models. ACA yields consistent performance increases on four tasks.

vs. 55.0% in S@3). This indicates that once the policy skeleton is consolidated, dedicating a minor portion of the budget to targeted Stage 2 mining provides larger marginal gains than further anchor repetition.

Performance Gains across Different VLAs. We evaluate the architectural compatibility of ACA by comparing adaptation gains on π_0 and $\pi_{0.5}$ backbones, as shown in Fig. 7. *(i) Architecture-agnostic efficacy.* ACA improves both models across all tasks, showing that the anchor-centric principle acts as a universal data-allocation strategy for flow-based VLAs. *(ii) Synergy with base capabilities.* While ACA enhances both models, the stronger $\pi_{0.5}$ achieves larger absolute gains, indicating that higher initial representation quality enables more effective anchor-based refinement.

6. Conclusion

We formalize the **Coverage–Density Trade-off** in VLA adaptation, identifying a **diversity trap** where excessive variety under strict budgets destabilizes learning, evidenced by a characteristic **inverted-U performance trend**. Our frame-

work, **Anchor-Centric Adaptation (ACA)**, operationalizes this insight by establishing a stable policy skeleton at anchors before expanding coverage via error-driven mining and constrained residuals. Real-robot experiments validate that ACA significantly improves task reliability, demonstrating that **structured repetition** is a more potent scaling lever than raw diversity for robust robotic deployment in data-scarce regimes. **Future Work.** Future research includes extending the anchoring principle to long-horizon manipulation via hierarchical decomposition and study autonomous anchor-discovery for resource optimization to scale generalizable skills across broader data distributions.

Acknowledgements

This research is supported by the National Research Foundation, Singapore under its AI Singapore Programme (AISG Award No: AISG3-RP-2022-030).

Impact Statement

This work provides a principled framework for the data-efficient adaptation of VLA models, enhancing the reliability and safety of embodied agents in data-scarce environments. By formalizing the Coverage–Density trade-off, ACA mitigates the risks of unpredictable behaviors caused by the diversity trap, ensuring more stable policy skeletons under limited human demonstrations. These contributions support the democratization of robotics, lowering the barrier for deploying high-performance foundation models in specialized, resource-constrained real-world applications.

References

- Ahn, M., Brohan, A., Brown, N., Chebotar, Y., Cortes, O., David, B., Finn, C., Fu, C., Gopalakrishnan, K., Hausman, K., et al. Do as i can, not as i say: Grounding language in robotic affordances. *arXiv preprint arXiv:2204.01691*, 2022.
- Bjorck, J., Castañeda, F., Cherniadev, N., Da, X., Ding, R., Fan, L., Fang, Y., Fox, D., Hu, F., Huang, S., et al. Gr00t n1: An open foundation model for generalist humanoid robots. *arXiv preprint arXiv:2503.14734*, 2025.
- Black, K., Brown, N., Driess, D., Esmail, A., Equi, M., Finn, C., Fusai, N., Groom, L., Hausman, K., Ichter, B., et al. π_0 : A vision-language-action flow model for general robot control. *arXiv preprint arXiv:2410.24164*, 2024.
- Black, K., Brown, N., Darpinian, J., Dhabalia, K., Driess, D., Esmail, A., Equi, M. R., Finn, C., Fusai, N., Galliker, M. Y., et al. $\pi_{0.5}$: a vision-language-action model with open-world generalization. In *9th Annual Conference on Robot Learning*, 2025.
- Bu, Q., Yang, Y., Cai, J., Gao, S., Ren, G., Yao, M., Luo, P., and Li, H. Univla: Learning to act anywhere with task-centric latent actions. *arXiv preprint arXiv:2505.06111*, 2025.
- Cen, J., Huang, S., Yuan, Y., Li, K., Yuan, H., Yu, C., Jiang, Y., Guo, J., Li, X., Luo, H., et al. Rynnvla-002: A unified vision-language-action and world model. *arXiv preprint arXiv:2511.17502*, 2025a.
- Cen, J., Yu, C., Yuan, H., Jiang, Y., Huang, S., Guo, J., Li, X., Song, Y., Luo, H., Wang, F., et al. Worldvla: Towards autoregressive action world model. *arXiv preprint arXiv:2506.21539*, 2025b.
- Chebotar, Y., Handa, A., Makoviychuk, V., Macklin, M., Issac, J., Ratliff, N., and Fox, D. Closing the sim-to-real loop: Adapting simulation randomization with real world experience. In *2019 International Conference on Robotics and Automation (ICRA)*, pp. 8973–8979. IEEE, 2019.
- Chen, X., Wei, H., Zhang, P., Zhang, C., Wang, K., Guo, Y., Yang, R., Wang, Y., Xiao, X., Zhao, L., et al. Villax: enhancing latent action modeling in vision-language-action models. *arXiv preprint arXiv:2507.23682*, 2025.
- Chopra, S., McMoil, A., Carnovale, B., Sokolson, E., Kubendran, R., and Dickerson, S. Everydayvla: A vision-language-action model for affordable robotic manipulation. *arXiv preprint arXiv:2511.05397*, 2025.
- Evans, L. C. *Partial differential equations*, volume 19. American mathematical society, 2022.
- Fei, S., Wang, S., Shi, J., Dai, Z., Cai, J., Qian, P., Ji, L., He, X., Zhang, S., Fei, Z., et al. Libero-plus: In-depth robustness analysis of vision-language-action models. *arXiv preprint arXiv:2510.13626*, 2025.
- Gao, C., Liu, Z., Chi, Z., Huang, J., Fei, X., Hou, Y., Zhang, Y., Lin, Y., Fang, Z., Jiang, Z., et al. Vlasos: Structuring and dissecting planning representations and paradigms in vision-language-action models. *arXiv preprint arXiv:2506.17561*, 2025.
- Garcia, R., Chen, S., and Schmid, C. Towards generalizable vision-language robotic manipulation: A benchmark and llm-guided 3d policy. In *2025 IEEE International Conference on Robotics and Automation (ICRA)*, pp. 8996–9002. IEEE, 2025.
- Hafez, M. B. and Wermter, S. Continual robot learning using self-supervised task inference. *IEEE Transactions on Cognitive and Developmental Systems*, 16(3):947–960, 2023.

- Hou, Z., Zhang, T., Xiong, Y., Duan, H., Pu, H., Tong, R., Zhao, C., Zhu, X., Qiao, Y., Dai, J., et al. Dita: Scaling diffusion transformer for generalist vision-language-action policy. *arXiv preprint arXiv:2503.19757*, 2025.
- Hu, E. J., Shen, Y., Wallis, P., Allen-Zhu, Z., Li, Y., Wang, S., Wang, L., Chen, W., et al. Lora: Low-rank adaptation of large language models. *ICLR*, 1(2):3, 2022.
- Jiang, Y., Cheng, S., Ding, Y., Gao, F., and Qi, B. Asyncvla: Asynchronous flow matching for vision-language-action models. *arXiv preprint arXiv:2511.14148*, 2025.
- Kachaev, N., Kolosov, M., Zelezetsky, D., Kovalev, A. K., and Panov, A. I. Don't blind your vla: Aligning visual representations for ood generalization. *arXiv preprint arXiv:2510.25616*, 2025.
- Kawaharazuka, K., Oh, J., Yamada, J., Posner, I., and Zhu, Y. Vision-language-action models for robotics: A review towards real-world applications. *IEEE Access*, 2025.
- Kim, M. J., Pertsch, K., Karamcheti, S., Xiao, T., Balakrishna, A., Nair, S., Rafailov, R., Foster, E., Lam, G., Sankeki, P., et al. Openvla: An open-source vision-language-action model. *arXiv preprint arXiv:2406.09246*, 2024.
- Kim, M. J., Finn, C., and Liang, P. Fine-tuning vision-language-action models: Optimizing speed and success. *arXiv preprint arXiv:2502.19645*, 2025.
- Lee, J., Duan, J., Fang, H., Deng, Y., Liu, S., Li, B., Fang, B., Zhang, J., Wang, Y. R., Lee, S., et al. Molmoact: Action reasoning models that can reason in space. *arXiv preprint arXiv:2508.07917*, 2025.
- Li, H., Zhang, I., Ouyang, R., Wang, X., Zhu, Z., Yang, Z., Zhang, Z., Wang, B., Ni, C., Qin, W., et al. Mimicdreamer: Aligning human and robot demonstrations for scalable vla training. *arXiv preprint arXiv:2509.22199*, 2025a.
- Li, Q., Liang, Y., Wang, Z., Luo, L., Chen, X., Liao, M., Wei, F., Deng, Y., Xu, S., Zhang, Y., et al. Cogact: A foundational vision-language-action model for synergizing cognition and action in robotic manipulation. *arXiv preprint arXiv:2411.19650*, 2024a.
- Li, Q., Deng, Y., Liang, Y., Luo, L., Zhou, L., Yao, C., Zeng, L., Feng, Z., Liang, H., Xu, S., et al. Scalable vision-language-action model pretraining for robotic manipulation with real-life human activity videos. *arXiv preprint arXiv:2510.21571*, 2025b.
- Li, W., Zhang, Q., Zhai, R., Lin, L., and Wang, G. Vla models are more generalizable than you think: Revisiting physical and spatial modeling. *arXiv preprint arXiv:2512.02902*, 2025c.
- Li, X., Hsu, K., Gu, J., Pertsch, K., Mees, O., Walke, H. R., Fu, C., Lunawat, I., Sieh, I., Kirmani, S., et al. Evaluating real-world robot manipulation policies in simulation. *arXiv preprint arXiv:2405.05941*, 2024b.
- Lin, F., Nai, R., Hu, Y., You, J., Zhao, J., and Gao, Y. Onetwovla: A unified vision-language-action model with adaptive reasoning. *arXiv preprint arXiv:2505.11917*, 2025.
- Lipman, Y., Chen, R. T., Ben-Hamu, H., Nickel, M., and Le, M. Flow matching for generative modeling. *arXiv preprint arXiv:2210.02747*, 2022.
- Liu, W., Zeng, W., He, K., Jiang, Y., and He, J. What makes good data for alignment? a comprehensive study of automatic data selection in instruction tuning. *arXiv preprint arXiv:2312.15685*, 2023.
- Mark, M. S., Gao, T., Sampaio, G. G., Srirama, M. K., Sharma, A., Finn, C., and Kumar, A. Policy agnostic rl: Offline rl and online rl fine-tuning of any class and backbone. *arXiv preprint arXiv:2412.06685*, 2024.
- Mu, Y., Zhang, Q., Hu, M., Wang, W., Ding, M., Jin, J., Wang, B., Dai, J., Qiao, Y., and Luo, P. Embodiedgpt: Vision-language pre-training via embodied chain of thought. *Advances in Neural Information Processing Systems*, 36:25081–25094, 2023.
- Ni, C., Chen, C., Wang, X., Zhu, Z., Zheng, W., Wang, B., Chen, T., Zhao, G., Li, H., Dong, Z., et al. Swiftvla: Unlocking spatiotemporal dynamics for lightweight vla models at minimal overhead. *arXiv preprint arXiv:2512.00903*, 2025.
- Niederreiter, H. *Random number generation and quasi-Monte Carlo methods*. SIAM, 1992.
- Nogueira, R. and Cho, K. Passage re-ranking with bert. *arXiv preprint arXiv:1901.04085*, 2019.
- O'Neill, A., Rehman, A., Maddukuri, A., Gupta, A., Padalkar, A., Lee, A., Pooley, A., Gupta, A., Mandlekar, A., Jain, A., et al. Open x-embodiment: Robotic learning datasets and rt-x models: Open x-embodiment collaboration 0. In *2024 IEEE International Conference on Robotics and Automation (ICRA)*, pp. 6892–6903. IEEE, 2024.
- Peng, X. B., Andrychowicz, M., Zaremba, W., and Abbeel, P. Sim-to-real transfer of robotic control with dynamics randomization. In *2018 IEEE international conference on robotics and automation (ICRA)*, pp. 3803–3810. IEEE, 2018.
- Pertsch, K., Stachowicz, K., Ichter, B., Driess, D., Nair, S., Vuong, Q., Mees, O., Finn, C., and Levine, S. Fast:

- Efficient action tokenization for vision-language-action models. *arXiv preprint arXiv:2501.09747*, 2025.
- Radford, A., Kim, J. W., Hallacy, C., Ramesh, A., Goh, G., Agarwal, S., Sastry, G., Askell, A., Mishkin, P., Clark, J., et al. Learning transferable visual models from natural language supervision. In *International conference on machine learning*, pp. 8748–8763. PmLR, 2021.
- Römer, R., Zhang, Y., and Schoellig, A. P. Clare: Continual learning for vision-language-action models via autonomous adapter routing and expansion. *arXiv preprint arXiv:2601.09512*, 2026.
- Shukor, M., Aubakirova, D., Capuano, F., Kooijmans, P., Palma, S., Zouitine, A., Aractingi, M., Pascal, C., Russi, M., Marafioti, A., et al. Smolvla: A vision-language-action model for affordable and efficient robotics. *arXiv preprint arXiv:2506.01844*, 2025.
- Sridhar, K., Dutta, S., Jayaraman, D., and Lee, I. Ricl: Adding in-context adaptability to pre-trained vision-language-action models. *arXiv preprint arXiv:2508.02062*, 2025.
- Tan, S., Dou, K., Zhao, Y., and Krähenbühl, P. Interactive post-training for vision-language-action models. *arXiv preprint arXiv:2505.17016*, 2025.
- Team, G. R., Abeyruwan, S., Ainslie, J., Alayrac, J.-B., Arenas, M. G., Armstrong, T., Balakrishna, A., Baruch, R., Bauza, M., Blokzijl, M., et al. Gemini robotics: Bringing ai into the physical world. *arXiv preprint arXiv:2503.20020*, 2025.
- Team, O. M., Ghosh, D., Walke, H., Pertsch, K., Black, K., Mees, O., Dasari, S., Hejna, J., Kreiman, T., Xu, C., et al. Octo: An open-source generalist robot policy. *arXiv preprint arXiv:2405.12213*, 2024.
- Wang, L., Zhang, K., Zhou, A., Simchowitz, M., and Tedrake, R. Robot fleet learning via policy merging. *arXiv preprint arXiv:2310.01362*, 2023.
- Wang, Y., Zhang, Y., Huo, M., Tian, R., Zhang, X., Xie, Y., Xu, C., Ji, P., Zhan, W., Ding, M., et al. Sparse diffusion policy: A sparse, reusable, and flexible policy for robot learning. *arXiv preprint arXiv:2407.01531*, 2024.
- Wen, J., Zhu, Y., Li, J., Zhu, M., Tang, Z., Wu, K., Xu, Z., Liu, N., Cheng, R., Shen, C., et al. Tinyvla: Towards fast, data-efficient vision-language-action models for robotic manipulation. *IEEE Robotics and Automation Letters*, 2025.
- Wu, Y., Wang, G., Yang, Z., Yao, M., Sheil, B., and Wang, H. Continually evolving skill knowledge in vision language action model. *arXiv preprint arXiv:2511.18085*, 2025.
- Xiang, T.-Y., Jin, A.-Q., Zhou, X.-H., Gui, M.-J., Xie, X.-L., Liu, S.-Q., Wang, S.-Y., Duan, S.-B., Xie, F.-C., Wang, W.-K., et al. Parallels between vla model post-training and human motor learning: Progress, challenges, and trends. *arXiv preprint arXiv:2506.20966*, 2025.
- Xue, Y., Lu, G., Wu, Z., Zhang, C., Jia, B., Gu, Z., Tang, Y., and Wang, Z. Resample: A robust data augmentation framework via exploratory sampling for robotic manipulation. *arXiv preprint arXiv:2510.17640*, 2025.
- Yang, R., Wei, H., Zhang, R., Feng, Z., Chen, X., Li, T., Zhang, C., Zhao, L., Bian, J., Su, X., et al. Beyond human demonstrations: Diffusion-based reinforcement learning to generate data for vla training. *arXiv preprint arXiv:2509.19752*, 2025.
- Yu, Z., Long, Y., Yang, Z., Zeng, C., Fan, H., Zhang, J., and Dong, H. Correctnav: Self-correction flywheel empowers vision-language-action navigation model. *arXiv preprint arXiv:2508.10416*, 2025.
- Zhang, B., Zhang, Y., Ji, J., Lei, Y., Dai, J., Chen, Y., and Yang, Y. Safevla: Towards safety alignment of vision-language-action model via constrained learning. *arXiv preprint arXiv:2503.03480*, 2025a.
- Zhang, D., Sun, J., Hu, C., Wu, X., Yuan, Z., Zhou, R., Shen, F., and Zhou, Q. Pure vision language action (vla) models: A comprehensive survey. *arXiv preprint arXiv:2509.19012*, 2025b.
- Zhang, H., Zhang, S., Jin, J., Zeng, Q., Li, R., and Wang, D. Robustvla: Robustness-aware reinforcement post-training for vision-language-action models. *arXiv preprint arXiv:2511.01331*, 2025c.
- Zhang, J., Chen, X., Wang, Q., Li, M., Guo, Y., Hu, Y., Zhang, J., Bai, S., Lin, J., and Chen, J. Vlm4vla: Revisiting vision-language-models in vision-language-action models. *arXiv preprint arXiv:2601.03309*, 2026.
- Zhang, W., Liu, H., Qi, Z., Wang, Y., Yu, X., Zhang, J., Dong, R., He, J., Lu, F., Wang, H., et al. Dreamvla: a vision-language-action model dreamed with comprehensive world knowledge. *arXiv preprint arXiv:2507.04447*, 2025d.
- Zhang, W., Wang, Y., Luo, H., Yuan, H., Feng, Y., Zheng, S., Jin, Q., and Lu, Z. Dig-flow: Discrepancy-guided flow matching for robust vla models. *arXiv preprint arXiv:2512.01715*, 2025e.
- Zhao, R., Ingebrand, T., Chinchali, S., and Topcu, U. Mosvla: A vision-language-action model with one-shot skill adaptation. *arXiv preprint arXiv:2510.16617*, 2025.

- Zheng, W., Li, B., Xu, B., Feng, E., Gu, J., and Chen, H. Leveraging os-level primitives for robotic action management. *arXiv preprint arXiv:2508.10259*, 2025.
- Zhong, Z., Yan, H., Li, J., Liu, X., Gong, X., Zhang, T., Song, W., Chen, J., Zheng, X., Wang, H., et al. Flowvla: Visual chain of thought-based motion reasoning for vision-language-action models. *arXiv preprint arXiv:2508.18269*, 2025.
- Zhu, F., Yan, Z., Hong, Z., Shou, Q., Ma, X., and Guo, S. Wmpo: World model-based policy optimization for vision-language-action models. *arXiv preprint arXiv:2511.09515*, 2025.
- Zhu, Y., Stone, P., and Zhu, Y. Bottom-up skill discovery from unsegmented demonstrations for long-horizon robot manipulation. *IEEE Robotics and Automation Letters*, 7(2):4126–4133, 2022.
- Zitkovich, B., Yu, T., Xu, S., Xu, P., Xiao, T., Xia, F., Wu, J., Wohlhart, P., Welker, S., Wahid, A., et al. Rt-2: Vision-language-action models transfer web knowledge to robotic control. In *Conference on Robot Learning*, pp. 2165–2183. PMLR, 2023.

A. Appendix



Figure 8. Visualization of real-robot rollouts across four tasks: from top to bottom, Block Stacking, Table Cleaning, Cup Placement, and Toy Tidying; each row shows the task instruction and corresponding key frames from the rollout video.

A.1. Analysis of the Coverage–Density Trade-off

This section provides comprehensive foundations for the Coverage–Density Trade-off presented in Section 3. We present: (i) complete proofs with detailed derivations; (ii) extensions to high-probability bounds; (iii) analysis of non-uniform allocation strategies; (iv) robustness analysis under assumption violations; (v) connections to optimal experimental design; and (vi) sample complexity lower bounds.

A.1.1. NOTATION AND PRELIMINARIES

We consolidate notation used throughout the theoretical analysis:

Table 3. Notation summary for theoretical analysis.

Symbol	Description
$\mathcal{P} \subset \mathbb{R}^d$	Condition parameter space (dimension d)
\mathcal{Z}	Action-state space
p, p_i	Condition parameters (queries and anchors)
z	Action-state variable
$t \in [0, 1]$	Flow time parameter
$f^*(z, p, t)$	Ground-truth conditional vector field
$\hat{f}(z, p, t)$	Learned/estimated vector field
N	Total sample budget
K	Number of distinct anchor conditions
n_i	Number of repeats at anchor p_i ($\sum_i n_i = N$)
h	Fill distance: $\sup_{p \in \mathcal{P}} \min_i \ p - p_i\ $
L	Lipschitz constant of f^* in p
Λ	Lipschitz constant of f^* in z
σ	Sub-Gaussian parameter of noise
C	Universal constant in estimation error bound
c	Constant in fill distance bound
δ	Confidence parameter for high-probability bounds

Sub-Gaussian Random Variables. A random variable X is σ -sub-Gaussian if for all $\lambda \in \mathbb{R}$,

$$\mathbb{E}[e^{\lambda X}] \leq e^{\sigma^2 \lambda^2 / 2}. \quad (18)$$

This implies the tail bound $\mathbb{P}(|X| \geq t) \leq 2e^{-t^2/(2\sigma^2)}$ and moment bound $\mathbb{E}[|X|^p]^{1/p} \leq C_p \sigma$ for constants C_p depending only on p .

Fill Distance and Covering. For a set of points $\{p_i\}_{i=1}^K \subset \mathcal{P}$, the fill distance quantifies worst-case coverage. For quasi-uniform placement (e.g., grid, low-discrepancy sequences (Niederreiter, 1992)), standard results give $h \asymp K^{-1/d}$ up to logarithmic factors.

A.2. Theory: Coverage–Density Trade-off

This section formalizes the coverage–density trade-off induced by a finite adaptation budget. The purpose of the analysis is not to claim that a generic neural policy is exactly a nearest-anchor estimator, but to isolate a statistically transparent mechanism: with a fixed number of demonstrations, increasing the number of task anchors improves coverage of the task-parameter space but reduces the number of samples available per anchor. We first prove this trade-off for a nearest-anchor surrogate, then state carefully what changes for stable interpolators, non-uniform allocation, discontinuous task regions, and two-stage sampling.

Notation. Let $\mathcal{P} \subset \mathbb{R}^d$ be a compact task-parameter domain equipped with norm $\|\cdot\|$. Let $\{p_i\}_{i=1}^K \subset \mathcal{P}$ be adaptation anchors and define the fill distance

$$h_K := \sup_{p \in \mathcal{P}} \min_{1 \leq i \leq K} \|p - p_i\|. \quad (19)$$

For each $p \in \mathcal{P}$, let

$$i(p) \in \arg \min_{1 \leq i \leq K} \|p - p_i\| \quad (20)$$

be an arbitrary nearest-anchor index. The target vector field or policy is denoted by $f^*(z, p, t)$, where z is the state or conditioning variable and $t \in [0, 1]$ is the flow-matching time variable. The learned predictor is \hat{f} . We write ξ for all sampling and optimization randomness used to construct \hat{f} . Unless otherwise stated, expectations are taken with respect to ξ and, when explicitly shown, a fixed evaluation distribution ν over (z, t) .

Assumptions. We use the following assumptions only where they are explicitly invoked.

Assumption A.1 (Lipschitz regularity in task parameter). There exists $L < \infty$ such that for all z, t , and $p, p' \in \mathcal{P}$,

$$\|f^*(z, p, t) - f^*(z, p', t)\| \leq L\|p - p'\|. \quad (21)$$

Assumption A.2 (Nearest-anchor surrogate). For the purpose of the baseline analysis, the predictor at an arbitrary task parameter uses the predictor at its nearest anchor:

$$\hat{f}(z, p, t) = \hat{f}(z, p_{i(p)}, t). \quad (22)$$

Assumption A.2 is deliberately restrictive. It should be read as defining an analyzable surrogate, not as a claim that the neural policy implemented in experiments is a nearest-neighbor rule. Extensions beyond this surrogate require additional stability assumptions and are discussed below.

A.2.1. COVERAGE-DENSITY DECOMPOSITION

Proposition A.3 (Coverage-density decomposition). *Suppose Assumptions A.1 and A.2 hold. Then for any evaluation distribution ν over (z, t) ,*

$$\sup_{p \in \mathcal{P}} \mathbb{E}_{(z,t) \sim \nu, \xi} [\|\hat{f}(z, p, t) - f^*(z, p, t)\|] \leq \max_{1 \leq i \leq K} \mathbb{E}_{(z,t) \sim \nu, \xi} [\|\hat{f}(z, p_i, t) - f^*(z, p_i, t)\|] + Lh_K. \quad (23)$$

The same inequality also holds pointwise for any fixed (z, t) if the expectation over $(z, t) \sim \nu$ is removed.

Proof. Fix any $p \in \mathcal{P}$ and any (z, t) . By Assumption A.2,

$$\hat{f}(z, p, t) = \hat{f}(z, p_{i(p)}, t). \quad (24)$$

The triangle inequality gives

$$\|\hat{f}(z, p, t) - f^*(z, p, t)\| \leq \|\hat{f}(z, p_{i(p)}, t) - f^*(z, p_{i(p)}, t)\| \quad (25)$$

$$+ \|f^*(z, p_{i(p)}, t) - f^*(z, p, t)\|. \quad (26)$$

Assumption A.1 and the definition of h_K imply

$$\|f^*(z, p_{i(p)}, t) - f^*(z, p, t)\| \leq L\|p_{i(p)} - p\| \leq Lh_K. \quad (27)$$

Taking expectation over ξ and optionally over $(z, t) \sim \nu$, then taking the supremum over p , yields (23). \square

Interpretation. The first term in (23) is a density term: it decreases when more samples are assigned to each anchor. The second term is a coverage term: it decreases when anchors form a finer cover of \mathcal{P} . The trade-off arises because, under a fixed total budget, increasing K improves h_K but reduces the sample count per anchor.

A.2.2. HIGH-PROBABILITY ANCHOR BOUND

The next result gives a high-probability version under an explicit repeated-query observation model. This model is intentionally stated narrowly: it applies to fixed (z, t) or to settings where anchor errors are already controlled uniformly over the relevant evaluation set. It should not be interpreted as a uniform guarantee over a continuous state-time space without an additional covering or function-class argument.

Assumption A.4 (Sub-Gaussian anchor observations). For a fixed (z, t) and each anchor p_i , suppose we observe

$$y_{ij} = f^*(z, p_i, t) + \varepsilon_{ij}, \quad j = 1, \dots, n_i, \quad (28)$$

where $\varepsilon_{ij} \in \mathbb{R}^m$ are independent, mean-zero, and coordinate-wise σ_i -sub-Gaussian. The anchor estimate is the sample mean

$$\hat{f}(z, p_i, t) = \frac{1}{n_i} \sum_{j=1}^{n_i} y_{ij}. \quad (29)$$

Lemma A.5 (Simultaneous concentration at anchors). *Under Assumption A.4, for any $\delta \in (0, 1)$, with probability at least $1 - \delta$, simultaneously for all anchors $i = 1, \dots, K$,*

$$\|\hat{f}(z, p_i, t) - f^*(z, p_i, t)\|_2 \leq \sigma_i \sqrt{\frac{2m \log(2mK/\delta)}{n_i}}. \quad (30)$$

For scalar outputs ($m = 1$), this reduces to

$$|\hat{f}(z, p_i, t) - f^*(z, p_i, t)| \leq \sigma_i \sqrt{\frac{2 \log(2K/\delta)}{n_i}}. \quad (31)$$

Proof. For any fixed anchor i and coordinate $r \in \{1, \dots, m\}$, the empirical mean error is $\sigma_i/\sqrt{n_i}$ -sub-Gaussian. Hence

$$\mathbb{P} \left(|\hat{f}_r(z, p_i, t) - f_r^*(z, p_i, t)| \geq \sigma_i \sqrt{\frac{2 \log(2mK/\delta)}{n_i}} \right) \leq \frac{\delta}{mK}. \quad (32)$$

A union bound over all mK coordinate-anchor pairs gives the coordinate-wise bound simultaneously. The Euclidean bound follows from $\|u\|_2 \leq \sqrt{m}\|u\|_\infty$. \square

Theorem A.6 (High-probability coverage–density bound). *Suppose Assumptions A.1, A.2, and A.4 hold for a fixed (z, t) . Let $n_{\min} := \min_i n_i$ and $\sigma_{\max} := \max_i \sigma_i$. Then with probability at least $1 - \delta$,*

$$\sup_{p \in \mathcal{P}} \|\hat{f}(z, p, t) - f^*(z, p, t)\|_2 \leq \sigma_{\max} \sqrt{\frac{2m \log(2mK/\delta)}{n_{\min}}} + Lh_K. \quad (33)$$

Proof. On the event of Lemma A.5, every anchor error is bounded by the first term in (33). Applying the deterministic triangle-inequality argument from Proposition A.3 gives the result. \square

A.2.3. OPTIMAL NUMBER OF ANCHORS UNDER UNIFORM ALLOCATION

Assume the anchors are quasi-uniform in the sense that for a geometry-dependent constant $c_{\mathcal{P}}$,

$$h_K \leq c_{\mathcal{P}} K^{-1/d}. \quad (34)$$

Assume further that a total budget N is split uniformly across anchors, so $n_i = N/K$, and that the expected anchor estimation error satisfies

$$\max_i \mathbb{E} \|\hat{f}(z, p_i, t) - f^*(z, p_i, t)\| \leq C\sigma \sqrt{\frac{K}{N}}. \quad (35)$$

Combining (23), (34), and (35) gives

$$\mathcal{E}(K) \leq C\sigma \sqrt{\frac{K}{N}} + Lc_{\mathcal{P}} K^{-1/d}. \quad (36)$$

The first term increases with K because each anchor receives fewer samples; the second term decreases with K because the anchor set covers \mathcal{P} more finely.

Ignoring integer constraints, minimizing the right-hand side of (36) yields

$$K^* \asymp \left(\frac{L^2 c_{\mathcal{P}}^2 N}{\sigma^2} \right)^{\frac{d}{d+2}}, \quad (37)$$

and the optimized error scales as

$$\mathcal{E}(K^*) \asymp (C\sigma)^{\frac{2}{d+2}} (Lc_{\mathcal{P}})^{\frac{d}{d+2}} N^{-\frac{1}{d+2}}. \quad (38)$$

With the high-probability bound in Theorem A.6, the same calculation holds up to logarithmic factors in K and $1/\delta$.

A.2.4. OPTIMAL NON-UNIFORM ALLOCATION

Uniform allocation is suboptimal when anchors have different noise levels or task difficulties. The following result characterizes the optimal allocation for minimizing the worst anchor-estimation term.

Proposition A.7 (Optimal non-uniform allocation). *Fix anchor locations $\{p_i\}_{i=1}^K$. Suppose the estimation error at anchor i is bounded by*

$$\frac{C\sigma_i}{\sqrt{n_i}}, \quad (39)$$

where $\sigma_i \geq 0$ and $\sum_{i=1}^K n_i = N$. If sample counts are allowed to be real-valued and at least one σ_i is nonzero, the allocation minimizing

$$\max_{1 \leq i \leq K} \frac{C\sigma_i}{\sqrt{n_i}} \quad (40)$$

is

$$n_i^* = N \frac{\sigma_i^2}{\sum_{j=1}^K \sigma_j^2}. \quad (41)$$

The achieved worst-anchor estimation error is

$$C \sqrt{\frac{\sum_{j=1}^K \sigma_j^2}{N}}. \quad (42)$$

Integer-valued allocations achieve the same rate up to rounding effects.

Proof. Let λ denote the value of the maximum. If

$$\max_i \frac{\sigma_i}{\sqrt{n_i}} \leq \lambda, \quad (43)$$

then necessarily $n_i \geq \sigma_i^2/\lambda^2$ for every i . Summing over i gives

$$N = \sum_i n_i \geq \frac{1}{\lambda^2} \sum_i \sigma_i^2, \quad (44)$$

so every feasible allocation satisfies

$$\lambda \geq \sqrt{\frac{\sum_i \sigma_i^2}{N}}. \quad (45)$$

The allocation (41) attains equality for every i with $\sigma_i > 0$, since

$$\frac{\sigma_i}{\sqrt{n_i^*}} = \sqrt{\frac{\sum_j \sigma_j^2}{N}}. \quad (46)$$

Multiplying by C gives (42). □

Implication. The optimal allocation is proportional to variance proxy σ_i^2 , not to standard deviation σ_i . Anchors with higher stochasticity require super-linear replication because the objective controls the worst anchor error.

A.2.5. BEYOND NEAREST-ANCHOR SURROGATES: STABLE INTERPOLATORS

The nearest-anchor analysis is conservative but does not automatically upper-bound an arbitrary neural network. A neural interpolator can be better or worse depending on optimization, regularization, representation, and extrapolation behavior. The following proposition states a sufficient condition under which the same type of decomposition applies.

Assumption A.8 (Predictor stability in task parameter). For a realized predictor \hat{f} , there exists $\hat{L} < \infty$ such that for all z, t and all $p, p' \in \mathcal{P}$,

$$\|\hat{f}(z, p, t) - \hat{f}(z, p', t)\| \leq \hat{L}\|p - p'\|. \quad (47)$$

Proposition A.9 (Coverage bound for stable interpolators). *Suppose Assumptions A.1 and A.8 hold. Then for any evaluation distribution ν over (z, t) ,*

$$\sup_{p \in \mathcal{P}} \mathbb{E}_{\nu, \xi} [\|\hat{f}(z, p, t) - f^*(z, p, t)\|] \leq \max_i \mathbb{E}_{\nu, \xi} [\|\hat{f}(z, p_i, t) - f^*(z, p_i, t)\|] + (L + \hat{L})h_K. \quad (48)$$

If \hat{L} is random, the same bound holds with $\mathbb{E}[\hat{L}]h_K$ after taking expectation, provided the stability condition holds almost surely.

Proof. For any p , let $i(p)$ be a nearest anchor. By the triangle inequality,

$$\|\hat{f}(z, p, t) - f^*(z, p, t)\| \leq \|\hat{f}(z, p_{i(p)}, t) - f^*(z, p_{i(p)}, t)\| \quad (49)$$

$$+ \|\hat{f}(z, p, t) - \hat{f}(z, p_{i(p)}, t)\| \quad (50)$$

$$+ \|f^*(z, p, t) - f^*(z, p_{i(p)}, t)\|. \quad (51)$$

The last two terms are bounded by $\hat{L}h_K$ and Lh_K , respectively. Taking expectations and the supremum over p proves the result. \square

Consequence for neural policies. Equation (48) is the appropriate formal way to relate neural interpolation to the coverage–density argument. Neural networks may have favorable empirical interpolation behavior, but an improved coverage term requires explicit smoothness or stability control. In particular, Lipschitz regularity of f^* alone supports an $O(h_K)$ worst-case coverage term; an $O(h_K^2)$ term requires stronger smoothness and an interpolation procedure with second-order approximation accuracy.

More generally, if an interpolator satisfies a deterministic approximation bound of order $\beta > 0$,

$$\sup_{p \in \mathcal{P}} \|\hat{f}(z, p, t) - f^*(z, p, t)\| \lesssim \max_i \|\hat{f}(z, p_i, t) - f^*(z, p_i, t)\| + Bh_K^\beta, \quad (52)$$

then the uniform-allocation trade-off becomes

$$\mathcal{E}_\beta(K) \lesssim C\sigma\sqrt{\frac{K}{N}} + BK^{-\beta/d}, \quad (53)$$

which is optimized at

$$K_\beta^* \asymp \left(\frac{B^2N}{\sigma^2}\right)^{\frac{d}{d+2\beta}}, \quad \mathcal{E}_\beta(K_\beta^*) \asymp \sigma^{\frac{2\beta}{d+2\beta}} B^{\frac{d}{d+2\beta}} N^{-\frac{\beta}{d+2\beta}}. \quad (54)$$

For the nearest-anchor/Lipschitz case, $\beta = 1$. A second-order rate $\beta = 2$ is possible only under stronger smoothness assumptions, such as bounded second derivatives in p , together with an interpolator that actually realizes second-order approximation.

A.2.6. ROBUSTNESS TO DISCONTINUITIES

Worst-case and average-case guarantees behave differently when the task map has discontinuities. A discontinuous region of small measure cannot improve a supremum bound: a worst-case query may still fall exactly in that region. Therefore measure-dependent robustness statements must be formulated for distributional risk.

Let μ be a test distribution over $p \in \mathcal{P}$. Suppose \mathcal{P} decomposes into a smooth region \mathcal{P}_{sm} and an exceptional region \mathcal{P}_{ex} such that

$$\mu(\mathcal{P}_{\text{ex}}) \leq \epsilon. \quad (55)$$

Assume f^* is L -Lipschitz on \mathcal{P}_{sm} , the anchors cover \mathcal{P}_{sm} with fill distance h_{sm} , and the loss is bounded on the exceptional region by M :

$$\mathbb{E}_{\nu, \xi} [\|\hat{f}(z, p, t) - f^*(z, p, t)\|] \leq M, \quad p \in \mathcal{P}_{\text{ex}}. \quad (56)$$

Then

$$\mathbb{E}_{p \sim \mu, (z, t) \sim \nu, \xi} [\|\hat{f}(z, p, t) - f^*(z, p, t)\|] \leq \max_i \mathbb{E}_{\nu, \xi} [\|\hat{f}(z, p_i, t) - f^*(z, p_i, t)\|] + Lh_{\text{sm}} + \epsilon M. \quad (57)$$

This bound is distributional. Without the expectation over $p \sim \mu$, the term ϵM cannot be used to control the supremum over all task parameters.

Practical implication. For contact-rich manipulation, discontinuities are best handled by phase segmentation, explicit mode-conditioned models, or additional anchors near suspected mode boundaries. The theory supports these interventions because they either reduce the smooth-region fill distance or reduce the probability mass and loss magnitude associated with exceptional regions.

A.2.7. HEAVY-TAILED NOISE

The sub-Gaussian assumption is convenient but may fail in robotics because rare catastrophic executions can produce heavy-tailed errors. The following statement gives a conservative expectation bound for the ordinary sample mean under finite-moment assumptions.

Proposition A.10 (Sample mean under finite moments). *Let $\varepsilon_1, \dots, \varepsilon_n$ be independent, mean-zero scalar random variables satisfying*

$$\mathbb{E}|\varepsilon_j|^q \leq \sigma^q \quad (58)$$

for some $q \in (1, 2]$. Then

$$\mathbb{E} \left| \frac{1}{n} \sum_{j=1}^n \varepsilon_j \right| \leq 2^{1/q} \sigma n^{-(1-1/q)}. \quad (59)$$

In particular, $q = 2$ recovers the usual $n^{-1/2}$ expectation rate, while the rate degrades as $q \downarrow 1$.

Proof. By Jensen's inequality,

$$\mathbb{E} \left| \frac{1}{n} \sum_{j=1}^n \varepsilon_j \right| \leq \left(\mathbb{E} \left| \frac{1}{n} \sum_{j=1}^n \varepsilon_j \right|^q \right)^{1/q}. \quad (60)$$

For $q \in (1, 2]$, the von Bahr–Esseen inequality gives

$$\mathbb{E} \left| \sum_{j=1}^n \varepsilon_j \right|^q \leq 2 \sum_{j=1}^n \mathbb{E}|\varepsilon_j|^q \leq 2n\sigma^q. \quad (61)$$

Therefore

$$\left(\mathbb{E} \left| \frac{1}{n} \sum_{j=1}^n \varepsilon_j \right|^q \right)^{1/q} \leq 2^{1/q} \sigma n^{1/q-1}, \quad (62)$$

which proves (59). \square

High-probability robustness. Under heavy-tailed noise, the ordinary sample mean generally does not satisfy the sub-Gaussian high-probability bound in Lemma A.5. If high-probability guarantees are required under only finite variance, the anchor estimator should be replaced by a robust mean estimator such as median-of-means or Catoni's estimator. Such estimators can recover $O(\sigma\sqrt{\log(1/\delta)/n})$ deviations under finite-variance assumptions, up to universal constants, but this requires changing the estimator.

A.2.8. TWO-STAGE CORE–BOUNDARY ALLOCATION

We next formalize the intuition behind a two-stage protocol. Unlike the main decomposition, this result depends on a stylized regional model. It should be interpreted as guidance for budget design, not as a claim that the empirical training pipeline exactly solves the corresponding optimization problem.

Suppose \mathcal{P} is partitioned into two regions,

$$\mathcal{P} = \mathcal{P}_{\text{core}} \cup \mathcal{P}_{\text{bd}}, \quad \mathcal{P}_{\text{core}} \cap \mathcal{P}_{\text{bd}} = \emptyset. \quad (63)$$

Let v_r denote the d -dimensional volume of region $r \in \{\text{core}, \text{bd}\}$, and let σ_r denote its noise scale. Assume region-specific anchor sets satisfy

$$h_r(K_r) \leq c_r \left(\frac{v_r}{K_r} \right)^{1/d}, \quad (64)$$

and that N_r samples are allocated to region r , uniformly over K_r anchors. The regional error model is

$$\mathcal{E}_r(K_r, N_r) \leq C\sigma_r \sqrt{\frac{K_r}{N_r}} + Lc_r \left(\frac{v_r}{K_r} \right)^{1/d}. \quad (65)$$

Proposition A.11 (Regional budget split under worst-case balancing). *Under the regional model (65), optimizing K_r within each region gives*

$$\mathcal{E}_r^*(N_r) \asymp (C\sigma_r)^{\frac{2}{d+2}} (Lc_r v_r^{1/d})^{\frac{d}{d+2}} N_r^{-\frac{1}{d+2}}. \quad (66)$$

If the objective is to minimize the maximum of the two regional errors, the balanced split satisfies

$$\frac{N_{\text{core}}}{N_{\text{bd}}} \asymp \frac{\sigma_{\text{core}}^2 c_{\text{core}}^d v_{\text{core}}}{\sigma_{\text{bd}}^2 c_{\text{bd}}^d v_{\text{bd}}}. \quad (67)$$

Proof. For fixed N_r , minimizing (65) over K_r is the same calculation as in (36), with $Lc_{\mathcal{P}}$ replaced by $Lc_r v_r^{1/d}$ and σ replaced by σ_r . This yields (66). To minimize the maximum regional error, the two optimized errors should be balanced unless one region receives a boundary allocation. Setting $\mathcal{E}_{\text{core}}^*(N_{\text{core}}) \asymp \mathcal{E}_{\text{bd}}^*(N_{\text{bd}})$ and raising both sides to the power $d+2$ gives

$$\frac{(C\sigma_{\text{core}})^2 (Lc_{\text{core}} v_{\text{core}}^{1/d})^d}{N_{\text{core}}} \asymp \frac{(C\sigma_{\text{bd}})^2 (Lc_{\text{bd}} v_{\text{bd}}^{1/d})^d}{N_{\text{bd}}}. \quad (68)$$

Canceling common constants gives (67). \square

Interpretation. For a worst-case objective, the split depends on region volume, geometry, and noise scale. Larger or geometrically harder regions require more coverage; noisier regions require more replication. If $c_{\text{core}} \approx c_{\text{bd}}$, the split simplifies to

$$\frac{N_{\text{core}}}{N_{\text{bd}}} \asymp \frac{v_{\text{core}}}{v_{\text{bd}}} \left(\frac{\sigma_{\text{core}}}{\sigma_{\text{bd}}} \right)^2. \quad (69)$$

Thus, a boundary region with larger noise can require a non-negligible fraction of the budget even if its volume is smaller. If the objective is average-case performance under a task distribution, the probability masses of the two regions also enter the allocation; the worst-case split above should then be modified accordingly.

A.2.9. RELATION TO STANDARD NONPARAMETRIC RATES

The rate in (38) is consistent with standard nonparametric regression over Lipschitz/Hölder classes. For a d -dimensional Lipschitz function class, the minimax integrated squared-error rate is of order

$$N^{-\frac{2}{d+2}}, \quad (70)$$

which corresponds to root mean-squared error of order

$$N^{-\frac{1}{d+2}}. \quad (71)$$

Our bound has the same exponent for the nearest-anchor Lipschitz case. The analysis here differs from classical nonparametric regression in that the design is summarized by anchor coverage and per-anchor replication, which makes the coverage–density trade-off explicit and directly interpretable for robotic adaptation.

A.2.10. CONNECTION TO NEURAL AND TRANSFORMER POLICIES

The formal results above do not require the deployed policy to be a nearest-neighbor rule. They instead provide a baseline decomposition that exposes what any successful interpolating policy must manage: anchor accuracy and task-space coverage.

For neural networks, the relevant question is whether training induces a stable interpolator in the task parameter. If the learned predictor has controlled Lipschitz constant in p , Proposition A.9 applies. If the task map is smoother than Lipschitz and the model realizes a higher-order approximation property, the generic β -order calculation predicts that fewer anchors may be required. However, such improvements are conditional on smoothness, optimization, and regularization; they are not implied by neural-network parametrization alone.

For transformer-based policies, attention can sometimes be interpreted as a learned kernel smoother over context examples or demonstrations. This interpretation is useful as intuition, but it does not by itself imply a coverage guarantee. A transformer may reduce interpolation error when its learned similarity metric aligns with the task geometry, but it may also extrapolate poorly outside the support of the adaptation data. Therefore, the formal theory should be read as an anchor-based statistical baseline, while the empirical results test whether the learned policy inherits the predicted qualitative behavior.

A.2.11. LIMITATIONS OF THE ANALYSIS

The analysis is intentionally conservative. Its guarantees are most informative when the following conditions approximately hold:

1. The task parameter p captures the dominant source of variation during adaptation.
2. The target map varies smoothly in p over the region being analyzed.
3. Anchor-level estimation error can be controlled through repeated or sufficiently similar samples.
4. The evaluation distribution over (z, t) is covered by the data used to estimate anchor predictors, or a separate common-support assumption is justified.

The guarantees may be loose or inapplicable when contact-mode discontinuities dominate, when state distributions shift substantially across task parameters, when failures induce heavy-tailed noise and the estimator is not robust, or when the neural policy has uncontrolled extrapolation behavior. These limitations motivate the practical design choices used in the method: phase-aware data collection, denser sampling near difficult regions, robust aggregation when failures are present, and a staged expansion from high-density core tasks to boundary tasks.

A.2.12. SUMMARY

The theory yields four main takeaways.

1. **Coverage–density decomposition.** Under Lipschitz regularity and a nearest-anchor surrogate, the error separates into an anchor-estimation term and a coverage term Lh_K .
2. **Interior optimum.** With a fixed budget N , increasing the number of anchors improves coverage but worsens per-anchor estimation. This yields an optimal scaling $K^* \asymp N^{d/(d+2)}$ in the Lipschitz case.
3. **Noise-aware allocation.** When anchor noise levels differ, worst-case estimation error is minimized by allocating samples proportional to σ_i^2 , not σ_i .
4. **Conditional extensions.** Stable neural interpolators satisfy analogous bounds with an explicit predictor-stability term. Higher-order coverage rates require stronger smoothness and approximation assumptions; they should not be claimed solely from using neural networks or transformers.